2016

Electronic structure of hydrothermally synthesized single crystal U0.22Th0.78O2

D. B. Turner

T. D. Kelly

G. R. Peterson

J. D. Reding

R. L. Hengehold

See next page for additional authors

Authors

D. B. Turner, T. D. Kelly, G. R. Peterson, J. D. Reding, R. L. Hengehold, J. M. Mann, J. W. Kolis, X. Zhang, Peter A. Dowben, and J. C. Petrosky

Phys. Status Solidi B **253,** No. 10, 1970–1976 (2016) / **DOI** 10.1002/pssb.201600277

physica status solidi b
www.pss-b.com
basic solid state physics

Electronic structure of hydrothermally synthesized single crystal $U_{0.22}Th_{0.78}O_2$

D. B. Turner*[,1], T. D. Kelly[2], G. R. Peterson[2], J. D. Reding[2], R. L. Hengehold[2], J. M. Mann[3], J. W. Kolis[4], X. Zhang[5], P. A. Dowben[5], and J. C. Petrosky[,2]**

[1] Oak Ridge Institute for Science and Education, 1299 Bethel Valley Road, Oak Ridge, TN 37830, USA
[2] Department of Engineering Physics, Air Force Institute of Technology, 2950 Hobson Way, WPAFB, OH 45433, USA
[3] Air Force Research Laboratory, Sensors Directorate, Wright-Patterson AFB, OH 45433, USA
[4] Department of Chemistry and Center for Optical Materials Science and Engineering Technologies (COMSET), Clemson University, Clemson, SC 29634-0973, USA
[5] Department of Physics and Astronomy, University of Nebraska-Lincoln, Theodore Jorgensen Hall, 855 North 16th Street, Lincoln, NE 68588-0299, USA

Received 2 May 2016, revised 20 June 2016, accepted 20 June 2016
Published online 7 July 2016

Keywords cathodoluminescence, electronic properties, inverse photoemission, ThO_2, ultraviolet photoemission, UO_2

* Corresponding author: e-mail david.turner@afit.edu, Phone: +1 937 255 3636 ext 4742, Fax: +1 937 656 6000
** e-mail james.petrosky@afit.edu

Single crystals of ThO_2, UO_2, and their solid solutions, $U_xTh_{1-x}O_2$, have been obtained through various hydrothermal growth conditions. This technique offers the better of two other growth processes: (i) single crystal purity as by photochemical growth of nanocrystals; and (ii) large/bulk sizes as obtained by the arc melt method. The band gap of the $U_xTh_{1-x}O_2$ single crystal solid solution, along with the luminescence transition, have been characterized. The occupied and unoccupied structures are determined using ultraviolet and inverse photoemission spectroscopy and the electronic band gap was measured to be 3–4 eV. The strain of incorporating U into the ThO_2 is analyzed through Vegard's law. In this crystal there are defect and impurity sites, likely arising from the kinetic growth process, giving rise to a similar yet slightly different optical gap evident with cathodoluminescence spectroscopy. There is a major luminescence feature spanning the range from 3.18 to 4.96 eV (250–390 nm) with a maximum at 4.09 eV (303 nm), corresponding with the measured electronic band gap. In this paper, the electronic properties of a solid solution $U_{0.22}Th_{0.78}O_2$ are measured and interpreted compared to the pure actinide oxides, ThO_2 and UO_2.

1 Introduction The next generation of nuclear power reactors will realize advances in fuel burn efficiency, environmental protection, and non-proliferation factors, culminating in the Generation-IV reactor classification. While many Generation-IV designs are being considered, most, if not all, have a closed fuel cycle to improve non-proliferation. Central to the issue of a closed fuel cycle are not only the obvious improvements in structural materials to withstand high pressures, temperatures, and chemical corrosion, but also advancements and improvements to useable nuclear fuels. Most of the world's current nuclear fuel technology consists of uranium dioxide and mixed uranium–plutonium oxide fuels. However, Generation-IV reactors require novel nuclear fuels to be developed, therefore, new alloys of oxides [1–3], carbides [4–7], and nitrides [8] are being considered. In particular, these fuel technologies are being studied down to the micrometer scale or smaller, where defects result in drastic changes in material characteristics, such as thermal and electronic performance or defect formation, clustering, and impurity migration under radiation.

Already, uranium–thorium dioxide alloys ($U_xTh_{1-x}O_2$) are of particular global interest as nuclear fuels due to their potential benefits in nuclear power and nuclear waste storage [9, 10] through the thorium fuel cycle. However, for their use in Generation-IV reactors, mixed oxide fuels may additionally exhibit beneficial physical and electronic properties that extend their usefulness beyond traditional nuclear fuel applications into regions such as nuclear detection, remote fuel burn up monitoring, and

radiation-hardened electronics by design. For example, initial theoretical results conclude that well-ordered mixed oxide fuels have reduced defect migration as in the case of the formation and mobility of He^{2+} ions [11, 12] and Xe (as a representative fission gas) [13]. Furthermore, experimental studies of colloids and ceramics indicate that the physical and electronic properties are variable (tunable) being extremely sensitive to material type and quality [14–20].

While ThO_2 and UO_2 single crystals have been previously synthesized [2, 3, 9, 21–33], the growth techniques did not provide the necessarily high quality combined with an appropriately "large" (ex. several millimeters) size suitable for spectroscopic analysis and device development while retaining a single crystal structure. For example, it has recently been demonstrated that nanocrystals of UO_2, ThO_2, and their solid solutions may be synthesized through low temperature (575–725 K) photochemical processes [3, 9, 21]. However, the crystal sizes are unsuitable for comparative studies of much larger, bulk mixed oxide fuels. On the other hand, larger single crystals of UO_2 have been synthesized through the traditional arc melt method [19, 20]. However this growth process results in crystals with thermal strain, high defect densities, and only short range order while allowing very little control in how these defects form and distribute themselves. From a review of these two growth processes, it is determined that temperature, pressure, and environmental conditions need to be precisely controlled in order to obtain large, single crystals of ThO_2, UO_2, and their solid solutions with well-resolved stoichiometry and limited defect density.

In the present research, a hydrothermal synthesis technique was developed [34, 35] and demonstrated to be suitable for quality ThO_2 crystal growth. This was followed by the synthesis and structural confirmation of $U_xTh_{1-x}O_2$ single crystal alloys [36]. While the ThO_2 single crystal band structure has been studied [37, 38], to our knowledge, the $U_xTh_{1-x}O_2$ has not been extensively studied beyond colloids, theoretical calculations, or cursory diffraction measurements [36]. Of particular interest is the role of the U 5*f* band when included into the ThO_2 matrix. Since ThO_2 is an n-type insulator with a band gap of 6–7 eV [38], and UO_2 is a large band gap semiconductor with its carrier type depending on temperature with localized *f*-electrons, it is desirable to determine how forming a solid solution of U within a ThO_2 matrix alters the resistive properties of the ThO_2 structure. The nature of the UO_2 5*f* electronic state's interactions with the ThO_2 matrix may be illuminated through a combination of traditional photoemission techniques [38, 39] combined with luminescence measurements. In this research, the fundamental band gap of a $U_xTh_{1-x}O_2$ single crystal solid solution is measured with ultraviolet and inverse photoemission spectroscopy. Then, the optical band gap and luminescence transitions are analyzed using cathodoluminescence spectroscopy. The results are important for establishing fundamental properties of single crystal $U_xTh_{1-x}O_2$ alloys that may then have their structural, thermal, and electronic properties tuned in order to understand their characteristics within extreme environments such as in next generation nuclear reactors.

2 Experimental

2.1 Crystal growth and preparation The $U_{0.22}Th_{0.78}O_2$ single crystal studied in this research was hydrothermally synthesized kinetically in a supercritical 9 M CsF mineralizer as detailed elsewhere [36]. The structure of $U_{0.22}Th_{0.78}O_2$ was confirmed as a fluorite crystal lattice through X-ray diffraction as previously for other refractory oxides grown through by this method, such as ThO_2 [34, 37] and HfO_2 [35]. The previous studies of ThO_2 obtained through this technique indicated that the surface can have near surface regions of impurity deposits resulting from cooling the hydrothermal solution. In order to remove these crystallite surface cations and anions resulting from the growth technique, an etching process was developed by our research group consisting of an organic solution of mixed crown ethers (15-crown-5, $[C_2H_4O]_5$ and 18-crown-6, $[C_2H_4O]_6$) and picric acid ($C_6H_3N_3O_7$). A 30 mM dichloromethane solution of crown ethers (1:1 molar ratio of $[C_2H_4O]_5$ and $[C_2H_4O]_6$) and a 22.6 mM $C_6H_3N_3O_7$(aq) solution was mixed with the crystal using a magnetic stir bar for 24 h which removed approximately 100 nm of the surface. Following this chemical etch, the crystal was baked in a vacuum desiccator for 16 h at 180 °C to limit hydration before subsequent measurements. The successfulness of the chemical etching was validated and confirmed by X-ray fluorescence spectroscopy using a Horiba XGT-7000 micro-XRF using a liquid nitrogen cooled Si(Li) detector.

2.2 Photoemission instrumentation Ultraviolet photoemission spectroscopy (UPS) and inverse photoemission spectroscopy (IPES) experiments were measured under ultrahigh vacuum conditions ($\sim 10^{-10}$ Torr). The UPS spectra were acquired with a SPECS PHOIBOS 150 CCD electron energy analyzer having an energy resolution of ~30 meV at room temperature when using the He(I) 21.2 eV emission line. While using the Omicron DAR 400 X-ray source, both the X-ray gun and sample were grounded to minimize sample surface charging effects, although surface charging may still have occurred without the use of a flood gun. The IPES measurements were obtained using a Kimball Physics ELG-2A-6299 electron gun and an OmniVac IPES 1000 solid state detector. In order to prevent system contamination from sputter etching the surface, the reported spectra are of "as grown" samples. Both UPS and IPES spectra have been aligned to the Fermi level, and binding energy spectra are plotted as E–E_F as previously for other materials such as ThO_2 [38], UO_2 [39], MoS_2:Na [40], and EuO:Gd [41].

2.3 Cathodoluminescent instrumentation The cathodoluminescence spectroscopy (CL) was measured under ultrahigh vacuum (1×10^{-8} Torr). The $U_{0.22}Th_{0.78}O_2$ sample was adhered to a Ta plate by spot welding strips of Ta wire with 99.95% purity across the sample. This plate

was attached to the copper sample holder which was then attached to the cold finger of a helium cryocooler mounted in the CL's primary ultrahigh vacuum chamber. The sample faced a quartz viewing window with the electron gun at an angle of 30° with respect to the plane of the crystal. The sample holder temperature was maintained at 36 K using a Leybold CoolPower 4.2 CGM liquid helium circulation cryocooler to control the temperature of the sample holder and sample inside the main chamber.

A Kimball Physics EMG-12 electron gun with a barium oxide cathode and a thoriated tungsten filament was operated between 0.50 and 20.0 keV. For this experiment, the electron gun was operated at 12 keV with a beam current of 10 μA, as verified with a Keithley 6458 picoammeter. The photons emitted from the cathodoluminescence relaxation process were focused into the slit of a Spex 500 M monochromator. The photon signal was then detected with an EMI C31034 photomultiplier tube in a Products For Research, Inc. cooled housing that was operated at −1200 V. The resolution of the CL system was approximately 0.05 nm over the wavelength range of 200–800 nm that was measured in these experiments. The spectra were measured at 36 K in order to increase luminescence and improve the signal to noise ratio.

3 Results and discussion

3.1 Occupied and unoccupied band structure results The measured photoemission intensites are plotted in Fig. 1 for both the occupied (a) and unoccupied (b) states, aligned to the Fermi energy. The red lines in Fig. 1 are pure Gaussian peaks with maximums placed at inflection points on the slopes of the lines in the ultraviolet photoemission (a) and inverse photoemission (b) spectra for determination of the band gap measurement. Although these experimental results are examining the electronic structure of a particular $U_xTh_{1-x}O_2$ solid solution ($x = 0.22$), at least three previous studies of the isomorphism moving from ThO_2 to UO_2 have been studied using X-ray diffraction [23, 42, 43] and extended X-ray absoprtion fine structure [43]. These studies concluded that structurally, the solid solutions $U_xTh_{1-x}O_2$ follow Vegard's law, with slight deviances in some cases (e.g., Ref. [42]) falling within the error of their experiments. Thus, while specific theoretical electronic calculations for our particular alloyed material do not exist, (aside from structural and thermodynamic calculations as in Ref. [44]), by studying the existing experimental and theoretical results for purely ThO_2 and UO_2 materials we may draw electronic conclusions concerning the solid solution of $U_{0.22}Th_{0.78}O_2$, assuming a "well-behaved" sample that follows Vegard's law.

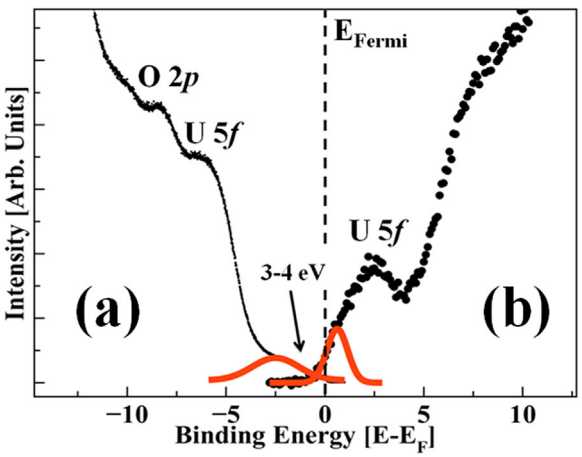

Figure 1 The experimental spectra for the (a) ultraviolet photoemission (occupied) and (b) inverse photoemission (unoccupied) states are plotted at normal incidence. Binding energies are referenced to the Fermi level as E–E_F. The difference in the red Gaussian peaks' maxima, placed at inflection points along the spectra, were used to measure the band gap.

In Table 1, experimental and theoretical results are listed for the band gap and weighted density of states (DOS) for the various electronic features of the actinide 5*f* and oxygen 2*p* concerning ThO_2 and UO_2 from the literature. These electronic properties are listed in units of eV. Although positive values are provided for the band gaps and DOS bandwidths, these are referenced with respect to the Fermi level E_F and provide information of the occupied DOS (not unoccupied). Most bandwidths provided for the 5*f* and 2*p* DOS are extracted from the data plots in the given reference, so should be considered as at least ±1 eV. Under the source type heading, either the experimental technique(s) are provided such as X-ray photoemission (XPS), ultraviolet photoemission (UPS), inverse photoemission (IPES), resonant photoemission (RPES), and X-ray absorption near edge structure (XANES) or the theoretical approach is indicated, such as molecular orbital (MO) theory or DFT calculation with the provided exchange-correlation functions used (e.g., GGA-PBE).

From Ref. [54], molecular orbital calculations were made using the self-consistent relativistic variation method on clusters of UO_8^{12-} with U–O distance 2.37 Å (the model is essentially a U atom surrounded by a simple cubic structure of O atoms). From these calculations for pure UO_2, the U 5*f* band is narrow and localized strongly near the Fermi edge, while the O 2*p* is more broadly found between 3.97 and 6.72 eV below the Fermi edge with strong O $2p_{3/2}$ signature at 5.69 eV.

The UPS and IPES spectra are plotted in Fig. 1, with the occupied (UPS) and unoccupied (IPES) 5*f* states labeled. If the UO_2 calculations were blindly applied to the solid solution measurements, then the experimental results plotted in Fig. 1 would appear to be missing the U 5*f* weighted density of states (DOS) as there is a gap between the Fermi edge and the first rising edge of the data. The calculations give insight into the approximate energies and order of the Th 6*d*, U 5*f*, and O 2*p* states. However, at least two considerations need to be made: (i) these are molecular orbital calculations and thus ignore the solid state intricacies that would be appropriate to studying a large single crystal;

Table 1 Computational and experimental measurements of ThO_2 and UO_2 band gaps.

actinide oxide	gap	actinide 5*f*	oxygen 2*p*	source type	year	reference
ThO_2	6–7	–	5.0–12.5	UPS/IPES	2014	[38]
	–	0.0–3.0	2.0–8.0	XANES	2014	[38]
	6.9	0.0–3.0	0.0–4.0	B3LYP	2013	[45]
	4.7	0.0–3.0	0.0– 4.0	LDA + U	2013	[45]
	4.5	–	–	LDA	2013	[45]
	4.43	–	–	GGA	2011	[46]
	4.637	0.0–3.79	0.0– 3.79	GGA	2010	[47]
	4.82	–	0.0– 5.0	GGA-92	2005	[48]
	5.0	–	2.0–7.0	RPES	1989	[49]
	5.0	–	0.0– 5.0	LMTO	1989	[49]
	6.0	???	???	???	1965	[50]
$U_{0.22}Th_{0.78}O_2$	3–4	3.0–7.0	6.0–11.0	UPS/IPES	2015	this study
UO_2	2.0	0.0–2.0	2.0–6.0	LDA + U	2013	[45]
	5.8	0.0–1.6	1.8–5.8	GGA-PBE	2010	[51]
	–	0.0–2.0	3.0–8.0	RPES	1987	[52]
	5.0 ± 0.4	0.0– 3.5	3.5–8.0	XPS/IPES	1980	[53]

and (ii) the UO_2 calculations ignore the existing ThO_2 matrix in which the U atoms exist.

The O 2*p* weighted DOS is at approximately 8.5 eV and the U 5*f* weighted DOS at approximately 2.5 eV below the Fermi level. This is notable as the appearance of strong U 5*f* character indicates the available valence states due to the U dopant are active within the ThO_2 matrix, although there is still an appreciable gap between the U 5*f* occupied and unoccupied states when compared to pure UO_2. Nevertheless, with the availability of the U 5*f* states, it is expected that the material may be electronically tuned if the oxidation state of the uranium dopant could be controlled during the hydrothermal synthesis. Similarly, the unoccupied character as probed by IPES is primarily of U 5*f* character, although U/Th 6*d* states are expected but not clearly evident in this case. The unoccupied structure begins at approximately 1.1 eV above the Fermi level, although as with the occupied structure, significant band tailing is evident and extends to approximately 0.1 eV below the Fermi level. From the molecular orbital diagrams of Teterin et al. on pure ThO_2 and UO_2 [54, 55] and the previous experimental of single crystal ThO_2 [38], the assignment of the U 5*f* states in the valence and conduction band can be made and is responsible for the smaller band gap than pure ThO_2 in this case.

We cannot exclude that a large number of defects and/or impurities, known to exist at such oxides surfaces in great abundance, contribute to significant band tailing, obscuring the actinide 6*d*/7*s* valence bands at the valence band maximum and the vertical binding energy of the unoccupied 5*f*/6*d* states that start at 1–2 eV above the Fermi level [38, 45]. An exact value for the band gap cannot be determined but is in the region 3–4 eV. This result is consistent with prior experimental measurements and theoretical calculations of UO_2 and ThO_2 as it lays between their reported 2–3 [51, 56, 57] and 6–7 eV [38, 45–47, 49, 50, 58, 59] band gaps, respectively.

3.2 Analysis of solid solution and Vegard's law Previously, structural measurements [36] indicated that U was incorporated into the ThO_2 following Vegard's Law, allowing for lattice constant interpolation. Similarly, Vegard's Law can be applied [60] to determine an interpolative scheme as

$$E_g(x) = xE_{g,UO2} + (1-x)E_{g,ThO2} - bx(1-x), \qquad (1)$$

where E_g is the band gap energy of $U_xTh_{1-x}O_2$, $E_{g,ThO2}$ is the band gap of ThO_2, $E_{g,UO2}$ is the band gap of UO_2, and b is the bowing parameter for $U_xTh_{1-x}O_2$. Using this research's measured band gap and information found in the literature for pure ThO_2 and UO_2 [38, 45–47, 49–51, 56–59], the band bowing parameter b is determined with and without including theoretical calculations. Including all references, the band bowing term is 6.0 ± 3.8 eV with estimates of the ThO_2 and UO_2 band gaps at 5.3 and 2.0 eV (± 0.2), respectively. Considering only the experimental data, the bowing term is 8.9 ± 3.1 eV with estimates of the ThO_2 and UO_2 band gaps at 5.8 and 2.2 eV (± 0.2), respectively, see Fig. 2. The larger difference in the ThO_2 band gap estimate may be attributed to the scattering of the experimental data. In all cases, experimental results are highly dependent on the material quality and type. Band gap information for fractional content x is lacking in the literature, consequently further research on similar alloys needs to be compiled in order to refine this first estimate of the band bowing term.

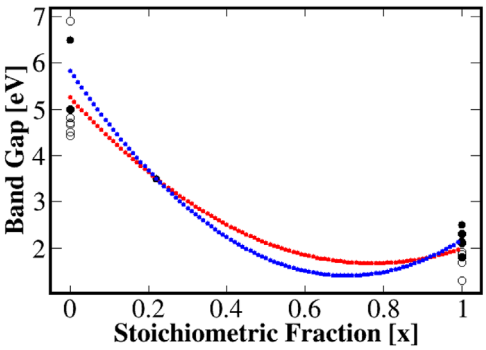

Figure 2 Theoretical values for ThO_2 ($x = 0$) and UO_2 ($x = 1$) band gap are plotted in open circles and experimental values as closed circles. The value at 0.22 is from this research, other values as referenced in text. Red dashed line is band gap from Eq. (1) accounting for all data; blue dashed line is only experimentally weighted.

While the band gap has been determined to be between 3 and 4 eV, a smaller functional gap due to the defects and impurities may be found through an optical technique such as photoluminescence or cathodoluminescence spectroscopy.

3.3 Cathodoluminscence results and analysis

For $U_{0.22}Th_{0.78}O_2$, the observed violet luminescence produced the spectrum in Fig. 3. The major peak of luminescence spans the region between 250 and 390 nm (3.18–4.96 eV) with a maximum at 303 nm (4.09 eV). The luminescence corresponds to the measured 3–4 eV band gap obtained from the combined UPS and IPES measurements. The dominant luminescence from the *f*-system crystals is assumed to be from the relaxation of an electron from the unoccupied U 5*f* state to the U 5*f* state within the valence band, and thus should frequently exceed the ground state band gap considerably. This transition is spin-forbidden and explains the low intensity of luminescence. As a comparison, under the same conditions of excitation, a single crystal of ThO_2 has 40 times the luminescence because the photon that is emitted comes from a spin-allowed or quadruple Th 6*d*/5*f* to O 2*p* transition [38].

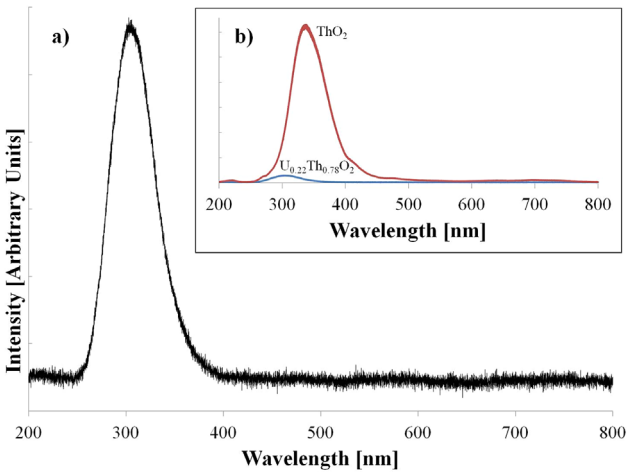

Figure 3 (a) Cathodoluminescence spectrum of $U_{0.22}Th_{0.78}O_2$ at 36 K. (b) Comparison of the cathodoluminescence intensities to display the differences between pure ThO_2 and $U_{0.22}Th_{0.78}O_2$.

4 Conclusions Single crystals of $U_{0.22}Th_{0.78}O_2$ have been investigated to characterize the valence and conduction band structure in the vicinity of the band gap. While pure ThO_2 has been shown to have partial 5*f* occupation [38], the addition of U into the ThO_2 matrix has resulted in measurable 5*f* character near the top of the valence band and splitting across the gap to the bottom of the conduction band, resulting in a reduction of the ThO_2 band gap from 6 to 7 eV to 3–4 eV.

Since the Fermi level does not lie in the center of the forbidden gap but closer to the conduction band minimum, these crystals are n-type. This result is consistent with previous studies on the band structure of ThO_2 [38]. Interestingly, this is not the case for polycrystalline samples of pure UO_2, which have been measured as p-type at room temperature, but becoming n-type at elevated temperatures ($\sim$1375 K). Of course, the UO_2 result is highly dependent on sample type and quality (e.g., polycrystalline, single crystal, glass) and that is the expected case here [16]. Considering the significant band tailing observed in the photoemission results and the broad spectral lines of the cathodoluminescence, it is expected that impurities and defects are largely responsible for the observed n-type behavior. Considering that the single crystals have been synthesized through a rapid growth process, the presence of structural defects is not surprising and defects have been noted in previous research [38]. We are assuming the same types of defects as in the case of the thorium dioxide single crystals because the two crystal systems were synthesized in very similar manners.

The incorporation of uranium into the thorium dioxide crystal matrix introduces U 5*f* states to the top of the valence band and bottom of the conduction band. The cathodoluminescence spectroscopy data aligns itself well with the data obtained from ultraviolet and inverse photoemission spectroscopy and the band gaps from each correspond with one another. The major luminescence peak from the $U_{0.22}Th_{0.78}O_2$ single crystal is broad and can be accounted for by intrinsic defects or due to the amount of hybridization between the orbitals. The luminescence from the $U_{0.22}Th_{0.78}O_2$ single crystal is weak due to the U 5$f^* \rightarrow$ U 5*f* transition which is believed to make up the majority of the character across the band gap [54, 55, 61]. However, due to the fact that the metals involve in this system are of such high Z in nature, the hybridization of the orbitals involved in the conduction band is significant. The luminescence emitted from this crystal system is greater than expected due to hybridization of the Th and U 6*d*, spin-allowed transition and Th and U 7*p*, quadrapole transition within the conduction band [38, 61]. With this progress in determining

the fundamental properties of mixed actinide oxide materials, studies may now be considered where there is a methodical and consistent effort to manipulate the defect densities.

Acknowledgements This work was supported by the Defense Threat Reduction Agency (grant no. HDTRA1-14-1-0041) and the Nebraska Materials Research Science and Engineering Center (NSF-DMR-1420645). The views expressed in this article are those of the authors and do not reflect the official policy or position of the United States Air Force, Department of Defense, or the U.S. Government.

References

[1] L. S. Natrajan, Coordin. Chem. Rev. **256**(15–16), 1583–1603 (2012).
[2] V. Tyrpek, J. Vigier, D. Manara, T. Wiss, O. D. Blanco, and J. Somers, J. Nucl. Mater. **460**, 200–208 (2015).
[3] T. Pavelkova, V. Cuba, and F. Sebesta, J. Nucl. Mater. **442**(1–3), 29–32 (2013).
[4] D. P. Daroca, A. M. Llois, and H. O. Mosca, J. Nucl. Mater. **460**, 216–220 (2015).
[5] D. P. Daroca, S. Jaroszewicz, A. M. Llois, and H. O. Mosca, J. Nucl. Mater. **454**(1–3), 217–222 (2014).
[6] D. P. Daroca, S. Jaroszewicz, A. M. Llois, and H. O. Mosca, J. Nucl. Mater. **437**(1–3), 135–138 (2013).
[7] Z. Liao, P. Huai, W. Qiu, X. Ke, W. Zhang, and Z. Zhu, J. Nucl. Mater. **454**(1–3), 142–148 (2014).
[8] S. Fujimori, T. Ohkochi, T. Okane, Y. Saitoh, A. Fujimori, H. Yamagami, Y. Haga, E. Yamamoto, and Y. Onuki, Phys. Rev. B **86**(23), 235108 (2012).
[9] T. Nenoff, B. Jacobs, D. Robinson, P. Provencio, J. Huang, S. Ferreira, and D. Hanson, Chem. Mater. **23**(23), 5185–5190 (2011).
[10] O. Roth, H. Hasselberg, and M. Jonsson, J. Nucl. Mater. **383**, 213–236 (2009).
[11] L. Dabrowski and M. Szuta, Nukleonika **57**(3), 337–343 (2012).
[12] M. Cooper, S. Murphy, P. Fossati, M. Rushton, and R. Grimes, Proc. R. Soc. A **470**, 20140427 (2014).
[13] Y. Yun, P. M. Oppeneer, H. Kim, and K. Park, Acta Mater. **57**, 1655–1659 (2009).
[14] D. Hudry, C. Apostolidis, O. Walter, T. Gouder, E. Coultois, C. Kubel, and D. Meyer, Chemistry **19**(17), 5297–5305 (2013).
[15] P. Ruello, G. Petot-Ervas, C. Petot, and L. Desgranges, J. Am. Ceram. Soc. **88**(3), 604–611 (2005).
[16] J. Killeen, J. Nucl. Mater. **88**, 185–192 (1980).
[17] J. Bates, C. Hinman, and T. Kawada, J. Am. Ceram. Soc. **50**(12), 652–656 (1967).
[18] H. Myers, T. Jonsson, and R. Westin, Solid State Commun. **2**(10), 321–322 (1964).
[19] T. Meek, B. von Roedern, and M. Haire, Trans. Am. Nucl. Soc. **88**, 416–418 (2003).
[20] T. T. Meek, B. von Roedern, P. Clem, and R. Hanrahan, Mater. Lett. **59**(8–9), 1085–1088 (2005).
[21] T. Nenoff, S. R. Ferriera, J. Huang, and D. J. Hanson, J. Nucl. Mater. **442**(1–3), 162–167 (2013).
[22] W. Hillerbrand, Bull. United States Geol. Survey **113**, 41 (1893).
[23] C. Herrick and R. Behrens, J. Cryst. Growth **51**, 183–189 (1981).
[24] D. Brit and H. Anderson, USAEC Technical Information Service **TID-7637**, 408 (1962).
[25] T. Sakurai, O. Kamada, and M. Ishigame, J. Cryst. Growth **2**, 326–327 (1968).
[26] R. Bard and D. Bowersox, United States Atomic Energy Commission [Unclassified and Declassified Reports Published by the Atomic Energy Commission and Its Contractors] **LA-2076**, 31 (1957).
[27] K. Kawabuchi and S. Magari, J. Cryst. Growth **49**, 81–84 (1980).
[28] S. Faile, J. Cryst. Growth **43**, 133–134 (1978).
[29] Y. Nomura, N. Kamegahira, and K. Naito, J. Cryst. Growth **52**, 279–284 (1981).
[30] K. Naito, N. Kamegashira, and Y. Nomura, J. Cryst. Growth **8**, 219–220 (1971).
[31] R. Singh and R. Coble, J. Cryst. Growth **21**, 261–266 (1974).
[32] W. Van Lierde, R. Strumane, E. Smets, and S. Amelinckx, J. Nucl. Mater. **5**(2), 250–253 (1962).
[33] R. Robins, J. Nucl. Mater. **3**(3), 294–301 (1961).
[34] M. Mann, D. Thompson, K. Serivalsatit, T. M. Tritt, J. Ballato, and J. Kolis, Cryst. Growth Des. **10**(5), 2146–2151 (2010).
[35] M. Mann and J. Kolis, J. Cryst. Growth **312**(3), 461–465 (2010).
[36] J. Castilow, T. W. Zens, J. M. Mann, J. W. Kolis, C. D. McMillen, and J. C. Petrosky, Mater. Res. Soc. Symp. Proc. **1576** (2013), doi: 10.1557/opl.2013.973.
[37] T. D. Kelly, J. C. Petrosky, J. W. McClory, T. W. Zens, D. Turner, J. M. Mann, J. W. Kolis, J. A. C. Santana, and P. A. Dowben, Mater. Res. Soc. Symp. Proc. **1576** (2013), doi: 10.1557/opl.2013.996.
[38] T. D. Kelly, J. C. Petrosky, D. Turner, J. W. McClory, J. M. Mann, J. W. Kolis, Xin Zhang, and P. A. Dowben, Phys. Status Solidi RRL **8**(3), 283–286 (2014).
[39] P. Roussel, P. Morrall, and S. J. Tull, J. Nucl. Mater. **385**, 53–56 (2009).
[40] K. Takashi, D. Le, X. Zhang, Q. Ma, E. Schwier, Y. Kojima, M. Zheng, H. Iwasawa, K. Shimada, M. Taniguchi, L. Bartels, T. S. Rahman, and P. A. Dowben, Appl. Phys. Lett. **105**(24), 241602 (2014).
[41] J. A. C. Santana, J. M. An, N. Wu, K. D. Belashchenko, X. Wang, P. Liu, J. Tang, Y. Losovyj, I. N. Yakovkin, and P. A. Dowben, Phys. Rev. B **85**(1), 014406 (2012).
[42] R. Bohler, A. Quaini, L. Capriotti, P. Cakir, O. Benes, K. Boboridis, A. Guiot, L. Luzzi, R. J. M. Konings, and D. Manara, J. Alloys Compd. **616**, 5–13 (2014).
[43] S. Hubert, J. Purans, G. Heisbourg, P. Moisy, and N. Dacheux, Inorg. Chem. **45**, 3887–3894 (2006).
[44] M. W. D. Cooper, S. T. Murphy, P. C. M. Fossati, M. J. D. Rushton, and R. W. Grimes, Proc. R. Soc. A **470**, 20140427 (2014), doi: 10.1098/rspa.2014.0427.
[45] B. Szpunar and J. A. Szpunar, J. Nucl. Mater. **439**, 243–250 (2013).
[46] A. Boudjemline, L. Louail, M. M. Islam, and B. Diawara, Comput. Mater. Sci. **50**, 2280–2286 (2011).
[47] B.-T. Wang, H. Shi, W.-D. Li, and P. Zhang, J. Nucl. Mater. **399**(2–3), 181–188 (2010).
[48] R. Terki, H. Feraoun, G. Bertrand, and H. Aourag, Comput. Mater. Sci. **33**, 44–52 (2005).

[49] W. P. Ellis, A. M. Boring, J. W. Allen, L. E. Cox, R. D. Cowan, B. B. Pate, A. J. Arko, and I. Lindau, Solid State Commun. **72**(7), 725–729 (1989).
[50] A. A. Sviridova and N. V. Suikovskaya, Opt. Spectrosc. **22**, 509 (1967).
[51] H. Shi, M. Chu, and P. Zhang, J. Nucl. Mater. **400**(2), 151–156 (2010).
[52] L. E. Cox, W. P. Ellis, R. D. Cowan, J. W. Allen, S. J. Oh, I. Lindau, B. B. Pate, and A. J. Arko, Phys. Rev. B **35**(11), 5761–5765 (1987).
[53] Y. Baer and J. Schoenes, Solid State Commun. **33**(8), 885–888 (1980).
[54] Y. A. Teterin and A. Y. Teterin, Nucl. Technol. Radiat. Protect. **29**(2), 3–13 (2004).
[55] Y. A. Teterin and A. Y. Teterin, Russ. Chem. Rev. **73**(6), 541–580 (2004).
[56] Q. Chen, X. Lai, T. Tang, B. Bai, M. Chu, Y. Zhang, and S. Tan, J. Nucl. Mater. **401**(1–3), 118–123 (2010).
[57] D. A. MacInnes and D. Martin, J. Nucl. Mater. **98**(3), 241–246 (1981).
[58] F. N. Skomurski, L. C. Shuller, R. C. Ewing, and U. Becker, J. Nucl. Mater. **375**(3), 290–310 (2008).
[59] B. Szpunar and J. A Szpunar, J. Phys. Chem. Solids **74**(11), 1632–1639 (2013).
[60] Y. Kuo, B. Liou, S. Yen, and H. Chu, Opt. Commun. **237**(4–6), 363–369 (2004).
[61] M. Ryzhkov and A. Kupryazhkin, J. Nucl. Mater. **384**(3), 226–230 (2009).

